International Journal of Thermophysics, Vol. 23, No. 1, January 2002 (© 2002)

Application of Neural Networks to a Predictive Extended Corresponding States Model for Pure Halocarbon Thermodynamics[1]

G. Scalabrin,[2, 3] L. Piazza,[2] and G. Cristofoli[2]

The extended corresponding states (ECS) model has been extensively studied for representing the thermodynamic surface of pure fluids and mixtures in the $a^R(\rho, T)$ form, and the most advanced version is currently the one for hydrofluorocarbons, but the shape factors $\vartheta(\rho, T)$ and $\varphi(\rho, T)$ have yet to be determined as analytical functions for the whole $P\rho T$ surface of a pure fluid. For a sample of pure halocarbons, this work aims to solve the fundamental problem of determining the individual shape functions over the entire $P\rho T$ domain through an innovative predictive procedure using a density model requiring only a single saturated liquid density input. An original algorithm using artificial neural networks enables the determination of the $\vartheta(\rho, T)$ and $\varphi(\rho, T)$ functions from *a priori* knowledge of their functional forms. The proposed algorithm focuses on the determination of the residual Helmholtz energy $a^R(\rho, T)$ for each fluid, subsequently allowing any other thermodynamic residual function to be calculated through the first and second derivatives of temperature and density. For each fluid studied, the model has been validated for residual functions against the same functions coming from highly accurate dedicated equations of state. The prediction accuracies reach average absolute deviation values ranging from 0.3 to 7.8%, spanning from vapor and liquid regions to supercritical conditions, while the corresponding results of the conventional ECS method range from 0.54 to 20%.

KEY WORDS: density; extended corresponding states; feedforward neural networks; fundamental equation of state; Helmholtz energy equation; refrigerants; residual functions.

[1] Paper presented at the Fourteenth Symposium on Thermophysical Properties, June 25–30, 2000, Boulder, Colorado, U.S.A.

[2] Dipartimento di Fisica Tecnica, Università di Padova, via Venezia 1, I-35131 Padova, Italy.

[3] To whom correspondence should be addressed. E-mail: gscala@unipd.it

0195-928X/02/0100-0057/0 © 2002 Plenum Publishing Corporation

1. INTRODUCTION

The theoretical background for corresponding states is based on a correspondence hypothesis for the potential energies of the components of a family of fluids [1, 2]. The fluids belonging to a family meeting this requirement are considered to share a condition of *conformality*, which implies a correspondence for the potential energies. This implies a correspondence of the $\psi(P, \rho, T)$ surfaces of each fluid, where P is the pressure, ρ is the density, and T is the temperature. Thus, if two fluids, i and j, belong to a conformal family, then

$$\psi_i \left[\left(\frac{P}{P_i^c} \right) \left(\frac{V}{V_i^c} \right) \left(\frac{T}{T_i^c} \right) \right] = \psi_j \left[\left(\frac{P}{P_j^c} \right) \left(\frac{V}{V_j^c} \right) \left(\frac{T}{T_j^c} \right) \right] = 0 \tag{1}$$

from which it follows that an f function,

$$P_r = f(T_r, V_r) \tag{2}$$

is the same for all the conformal fluids. In Eqs. (1) and (2), V is the volume, while the superscript c and the subscript r indicate the critical and reduced values, respectively.

Then all the derived residual state functions are also conformal. In particular, it has been demonstrated through further developments of statistical mechanics theory [3–5] that the fundamental conformality condition can be reduced to the following relation:

$$a_j^R(\rho_j, T_j) = a_i^R(\rho_i, T_i) = a_i^R \left(\frac{\rho_j}{\rho_j^c} \rho_i^c, \frac{T_j}{T_j^c} T_i^c \right) \tag{3}$$

where a^R is the reduced residual Helmholtz free energy. It has been shown that this relation is not satisfied even for the noble gases and the fluids considered here. A correction to this model is consequently needed, the details of which are shown later. Nonetheless, knowledge of the $\psi(P, \rho, T)$ surfaces is now available, with the highest possible accuracy, from a dedicated equation of state (DEoS) according to the Schmidt–Wagner technique [6]. The fluids considered in this study are reported in Table I, together with the limits of validity of their DEoS. First, two grids in the independent T_r and P_r variables were set up with the steps indicated in Table II for artificial neural network (ANN) training and validation, respectively. The training set numbers approximately 600 points in all, while the validation set is composed of more than 5000 points. The ranges of T_r and P_r were then selected for each fluid to observe the single range of validity for the DEoS (Table I).

Table I. Dedicated Equations of State and Ranges of Validity for the Halocarbon Fluids Considered

Fluid	Formula	T_r min	T_r max	P_r max	Ref. no.
R11	CCl_3F	0.34	1.33	6.8	[15]
R12	CCl_2F_2	0.45	1.56	17.0	[16]
R22	$CHClF_2$	0.31	1.49	12.0	[17]
R32	CH_2F_2	0.45	1.43	10.3	[18]
R123	$CHCl_2CF_3$	0.36	1.15	10.9	[19]
R125	CHF_2CF_3	0.51	1.47	18.7	[18]
R134a	CH_2FCF_3	0.45	1.34	17.3	[20]
R152a	CH_3CHF_2	0.40	1.13	6.7	[21]

2. EXTENDED CORRESPONDING STATES (ECS) IDENTITIES

According to classical ECS theory, two fluids are considered conformal if they obey the following condition:

$$a_j^R(\rho_j, T_j) = a_0^R(\rho_0, T_0) \tag{4}$$

in which subscripts 0 and j stand for the reference fluid and the fluid of interest, respectively. A DEoS of the $a_0^R(\rho, T_0)$ form is then needed for the reference fluid.

In a two-parameter corresponding states framework, the condition of Eq. (4) would be satisfied by "distorting" the independent variables through the constant *scale factors* h_j and f_j:

$$T_0 = \frac{T_j}{f_j}, \qquad f_j = \left(\frac{T_j^c}{T_0^c}\right); \qquad \rho_0 = \rho_j h_j, \qquad h_j = \left(\frac{\rho_0^c}{\rho_j^c}\right) \tag{5, 6}$$

Table II. Training and Validation Grid Steps for T_r and P_r

	Vapor	Liquid	Supercritical
T_r step			
Training	0.02	0.02	0.02
Validation	0.01	0.01	0.01
P_r step			
Training	0.05	0.5	0.5
Validation	0.01	0.1	0.1

As mentioned, this is not sufficient for the real fluids and a further correction to the former "distortion" has to be introduced by means of the shape factors $\theta_j(\rho_j, T_j)$ and $\phi_j(\rho_j, T_j)$:

$$f_j = \left(\frac{T_j^c}{T_0^c}\right)\theta_j(\rho_j, T_j), \qquad h_j = \left(\frac{\rho_0^c}{\rho_j^c}\right)\phi_j(\rho_j, T_j) \tag{7, 8}$$

From the fundamental relation, Eq. (4), the formalism to obtain any thermodynamic property can now be developed. Restricting our attention to the more frequently applied thermodynamic functions, the following identities are valid:

$$Z_j^R = u_0^R F_\rho + Z_0^R(1 + H_\rho) \tag{9}$$

$$u_j^R = u_0^R(1 - F_T) - Z_0^R H_T \tag{10}$$

$$s_j^R = s_0^R - u_0^R F_T - Z_0^R H_T \tag{11}$$

$$h_j^R = h_0^R + u_0^R(F_\rho - F_T) + Z_0^R(H_\rho - H_T) \tag{12}$$

$$g_j^R = g_0^R + Z_0^R H_\rho + u_0^R F_\rho \tag{13}$$

with

$$F_T = \left(\frac{\partial f_j}{\partial T_j}\right)_{\rho_j}\left(\frac{T_j}{f_j}\right), \qquad F_\rho = \left(\frac{\partial f_j}{\partial \rho_j}\right)_{T_j}\left(\frac{\rho_j}{f_j}\right) \tag{14, 15}$$

$$H_T = \left(\frac{\partial h_j}{\partial T_j}\right)_{\rho_j}\left(\frac{T_j}{h_j}\right), \qquad H_\rho = \left(\frac{\partial h_j}{\partial \rho_j}\right)_{T_j}\left(\frac{\rho_j}{h_j}\right) \tag{16, 17}$$

3. NEURAL NETWORKS

A new model is proposed here, based on the combination of ECS theory with ANN. Neural networks are versatile function approximators. They represent a simplified model of the basic architecture of the human brain and have been developed in the context of artificial intelligence studies since 1950 [7]. A milestone in this field is the work by Rumelhart and Mc Lelland [8], which overcame some shortcomings of the earlier ANN.

One of the most used types of ANN is multilayer feedforward neural networks (MLFN); see Fig. 1. They are formed by three layer of neurons. The first layer (input layer) receives the scaled inputs (independent variables) of the system; the last (output layer) gives the answer, or answers, of the system to the input stimulation. The hidden layer performs the elaboration of the final outputs from input signals, through nonlinear

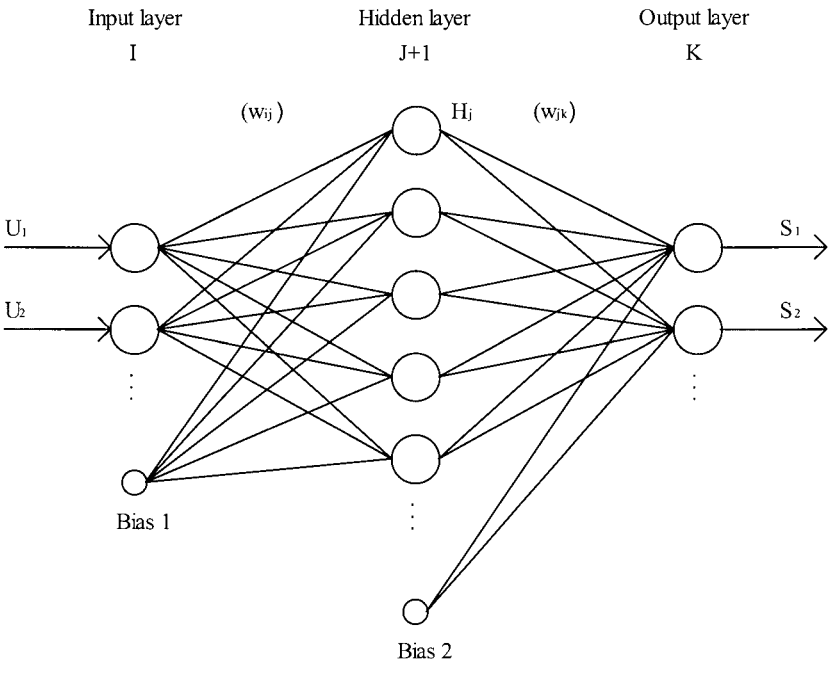

Fig. 1. Three-layer feedforward neural network architecture.

analytical operations. An ANN's domain and codomain can be multidimensional; in other words, an ANN can have multiple inputs and multiple outputs.

In the last decades, MLFNs have been applied to a wide number of problems. Limiting our attention to the field of thermophysical properties, they have been used for prediction of the volumetric properties of gases [9] and of two-phase mixtures [10], for prediction of the vapor pressure of pure fluids [11] and of the vapor–liquid equilibrium (VLE) of asymmetric mixtures [12], and for prediction of the liquid viscosity, density, heat of vaporization, boiling point, and Pitzer's acentric factor of pure fluids [13].

It has been demonstrated that an ANN is able to approximate any continuous function in a compact domain [14]. We have chosen to represent both of the *shape factors* by means of a single MLFN with two outputs, i.e., the shape factor functions, Eqs. (7) and (8), since these take effect simultaneously, distorting the independent variables that enter the reference fluid DEoS, Eq. (4). The ANN are used here to represent the shape factors $\vartheta_j = \vartheta_j(T_{r,j}, \delta_j)$ and $\phi_j = \phi_j(T_{r,j}, \delta_j)$ as functions of the independent variables $(T_{r,j}, \delta_j)$.

Referring to Fig. 1, the two values of the input layer, U_1 and U_2, represent the scaled independent thermodynamic variables, related, respectively, to the reduced temperature and to the reduced density. The two values of the output layer, S_1 and S_2, represent the scaled shape factors $\vartheta_j = \vartheta_j(T_{r,j}, \delta_j)$ and $\phi_j = \phi_j(T_{r,j}, \delta_j)$. As in the current practice of ANN, both input layer values, U_1 and U_2, and output layer values, S_1 and S_2, are compressed here within the same range, 0.05 to 0.95. This means that U_1 and U_2 do not coincide with the "true" independent variables $(T_{r,j}, \delta_j)$ but represent a linear transformation of them. Correspondingly, S_1 and S_2 are linear transformations of the two actual outputs ϑ_j and ϕ_j.

Each neuron of a layer takes the weighted summation of all the neurons in the previous layer and then passes this summation through a transfer function. The transfer function used here is a sigmoid function of the form

$$f(x) = \alpha \frac{1}{1+e^{-2\beta x}} \tag{18}$$

Two parameters have been applied in Eq. (18) to make the function's behavior more flexible: α changes the activation span and β determines the steepness of the sigmoid function. Our choice is to set them as $\alpha = 1.0$ and $\beta = 0.005$.

The ANN topology is determined once the number of neurons in the three layers is fixed: I represents the number of neurons in the input layer (including a bias term), and K is the number of neurons in the output layer. In our case, there are two inputs and two outputs, so $I = 3$ and $K = 2$.

The number of neurons in the hidden layer J (bias not included) has to be found by trial- and- error. In this case the value $J = 7$ was an ideal compromise between computation speed and accuracy of the resulting function. Bias nodes are not necessary, but they are introduced to increase the speed of the training process. They are constant and are here set to

$$\text{Bias } 1 = 1.0, \qquad \text{Bias } 2 = 1.0$$

The scaling of input and outputs in the range 0.05 to 0.95 is accomplished by setting

$$A_{\min} = 0.05, \qquad A_{\max} = 0.95$$

The following equations represent the neural network analytical formulation:

$$u_i = \frac{A_{\max} - A_{\min}}{V_{\max,i} - V_{\min,i}}, \qquad 1 \leqslant i \leqslant I-1 \tag{19}$$

$$s_k = \frac{A_{\max} - A_{\min}}{W_{\max,k} - W_{\min,k}}, \qquad 1 \leqslant k \leqslant K \tag{20}$$

$$W_k = \frac{S_k - A_{\min}}{s_k} + W_{\min,k}, \qquad 1 \leqslant k \leqslant K \tag{21}$$

$$S_k = f\left(\sum_{j=1}^{J+1} w_{jk} H_j\right), \qquad 1 \leqslant k \leqslant K \tag{22}$$

$$H_j = f\left(\sum_{i=1}^{I} w_{ij} U_i\right), \qquad 1 \leqslant j \leqslant J \tag{23}$$

$$H_{J+1} = \text{Bias 2}$$

$$U_i = u_i(V_i - V_{\min,i}) + A_{\min}, \qquad 1 \leqslant i \leqslant I-1 \tag{24}$$

$$U_I = \text{Bias 1}$$

In Eqs. (22) and (23) the transfer function defined in Eq. (18) is recalled. In Eq. (22) the summation is over the $J+1$ nodes of the hidden layer, and in Eq. (23) it is over the I nodes of the input layer. In our case the actual inputs V_1 and V_2 represent the independent variables of the system:

$$V_1 = T_{r,j}, \qquad V_2 = \delta_j = (\rho/\rho^c)_j$$

and similarly, the actual outputs W_1 and W_2 represent the dependent variables:

$$W_1 = \vartheta_j(T_{r,j}, \delta_j), \qquad W_2 = \phi_j(T_{r,j}, \delta_j)$$

The following parameters have to be defined according to the specific problem to solve. $V_{\min,i}$ and $V_{\max,i}$ are the limits of the independent input variables for the training set; $W_{\min,k}$ and $W_{\max,k}$ are the limit values of the shape factors, which, in this case, were set between 0.8 and 1.2. Due to the general form of the MLFN selected for application to the present problem (Fig. 1), the ANN weighting factors are 21 for the first matrix, w_{ij}, and 16 for the second matrix, w_{jk}, for a total of 37 weighting factors. The values of the weighting factor matrixes, w_{ij} and w_{jk}, are the ECS–NN EoS parameters, i.e., the unknowns of the proposed EoS, which have to be obtained individually for each fluid of interest through an optimization procedure [22] which aims at the minimization of an objective function. For the

optimization, a quasi-Newton method was applied and the software was written by the authors.

Once the training has been done, for each fluid the shape factors $\vartheta_j = \vartheta_j(T_{r,j}, \delta_j)$ and $\phi_j = \phi_j(T_{r,j}, \delta_j)$ are obtained in continuous form, and through Eqs. (4)–(17) the thermodynamic properties of interest can be computed.

4. MLFN FUNCTION APPROXIMATOR TESTING

First, we verified the ability of this model to approximate the fundamental thermodynamic function $a_j^R(T_j, \rho_j)$ of one of the fluids considered. We selected R134a as the reference fluid and chose to approximate the $a_j^R(T_j, \rho_j)$ DEoS function of R32. We generated $a_j^R(T_j, \rho_j)$ data from the R32 DEoS in vapor, liquid, and supercritical zones, as specified in Section 2, and then trained the network with these data. The objective function assumed was

$$f_{\text{ob, 1}} = \frac{1}{n} \sum_{i=1}^{n} \left[\frac{(a_j^R)_i^{\text{exp}} - (a_j^R)_i^{\text{calc}}}{(a_j^R)_i^{\text{exp}}} \right]^2 \tag{25}$$

The $a_j^R(T_j, \rho_j)$ ECS–NN EoS obtained was tested against the above validation set, demonstrating that the original data were globally approximated with an average absolute deviation (AAD) of less than 0.3% in the a^R values. The model can thus approximate the fundamental thermodynamic function $a_j^R(T_j, \rho_j)$ to a very good degree, even for the most difficult fluid to represent among those considered here, as explained below.

5. REGRESSION OF A MLFN ON GENERATED DENSITY DATA

Neural shape factors can be determined not only from $a_j^R(T_j, \rho_j)$ data, but also from any kind of thermodynamic value, providing the appropriate ECS identity is given, e.g., Eqs. (4) and (9) to (13). We implemented the regression of $P\rho T$ data in the three zones and on the saturation line. We used a DEoS to generate a set of $P\rho T$ points in the vapor, liquid, and supercritical regions and on the saturation line. This training set numbers approximately 600 points in the three regions and is described in Section 2. For the bulk-phase regression we considered the following objective function,

$$f_{\text{ob, 2}} = \frac{1}{n} \sum_{i=1}^{n} \left[\frac{(Z_j^R)_i^{\text{exp}} - (Z_j^R)_i^{\text{calc}}}{(Z_j^R)_i^{\text{exp}}} \right]^2 \tag{26}$$

where $(Z_j^R)^{\text{calc}}$ is given by Eq. (9), while at saturation a second objective function was considered,

$$f_{\text{ob, 3}} = \frac{1}{n} \sum_{i=1}^{n} [(\ln \varphi_j)_i^{sl} - (\ln \varphi_j)_i^{sv}]^2 \tag{27}$$

where $\ln \varphi_j$ is given by Eq. (28) combined with Eq. (13):

$$\ln \varphi = g^R - \ln Z \tag{28}$$

The EoS parameter optimization process was developed using an overall objective function which was selected as a linear combination of the two former functions, Eqs. (26) and (27):

$$f_{\text{ob, overall}} = 0.9 f_{\text{ob, 2}} + 0.1 f_{\text{ob,3}} \tag{29}$$

After training the network, we tested the model's ability to reproduce the fundamental thermodynamic function $a_j^R(T_j, \rho_j)$ and its first partial derivatives related to $Z_j^R(T_j, \rho_j)$ and $u_j^R(T_j, \rho_j)$. The results are listed in Table III. Looking at the case for R32, which was formerly studied for the $a_j^R(T_j, \rho_j)$ function approximation, its weighted average error deviation for the three regions was 0.4. This figure is only slightly higher than the 0.3 in the former case, so the ECS–NN EoS can be trained on a derived quantity, such as density, without any substantial loss of accuracy on the fundamental surface $a_j^R(T_j, \rho_j)$. The u^R function, which is related to a^R through the temperature first derivative of the shape factors, Eqs. (10), (14), and (16), can also be represented well.

We then tested the model for the prediction of $Z_j(T_j, P_j)$, $a_j^R(T_j, P_j)$, $u_j^R(T_j, P_j)$, $h_j^R(T_j, P_j)$, $s_j^R(T_j, P_j)$, $g_j^R(T_j, P_j)$, and $\ln \varphi_j(T_j, P_j)$. An inversion is always needed for practical uses, due to the default choice of T and P as independent variables. The different choice of independent variables in this second case demands an iterative procedure to find a solution for $\rho_j(T_j, P_j)$. The results of the validation study are listed in Table IV. The accuracy of the volumetric model can be evaluated through the $Z_j(T_j, P_j)$ function; the AAD achieved is comparable with the corresponding value of a Schmidt–Wagner multiparameter DEoS. The residual functions are also well represented, with s^R deviating in the vapor phase at a maximum of 4.15% with respect to a DEoS, whose error deviation for this function (and for some others) is unknown. It is worth emphasizing that the upper limit of the liquid phase was globally less than 1%.

Finally, as proof of its consistency, saturation pressures and saturated liquid and vapor densities were calculated from the model through the VLE

Table III. Residual Functions' Prediction Accuracy Without Inversion for ECS–NN Trained on Data Generated from DEoS

		AAD (%)		
Property	Fluid	Vapor	Liquid	Supercritical
a^R	R11	0.967	0.157	1.593
	R22	0.445	0.054	0.456
	R32	1.071	0.088	0.383
	R123	0.520	0.236	0.197
	R125	0.603	0.237	2.032
	R152a	0.935	0.142	0.525
	Avg.	0.757	0.151	0.982
Z^R	R11	1.395	0.429	2.069
	R22	0.817	0.258	1.444
	R32	0.980	0.223	1.431
	R123	0.849	0.287	0.986
	R125	0.958	0.371	1.772
	R152a	0.983	0.321	0.950
	Avg.	1.000	0.315	1.555
u^R	R11	3.474	0.619	2.867
	R22	2.220	0.238	0.662
	R32	2.309	0.328	1.577
	R123	1.726	0.482	0.589
	R125	3.488	0.465	4.709
	R152a	2.179	0.259	0.2943
	Avg.	2.571	0.398	2.103
	Overall	1.443	0.288	1.547

condition, $\varphi_{sl} = \varphi_{sv}$, on the saturation line. The results are presented in Table V. These three values have to be considered as the residual deviation errors for the final EoS, because all three were used in the minimization objective function.

6. REGRESSION OF A MLFN ON DATA FROM A PREDICTIVE VOLUMETRIC MODEL

In this case, the ECS–NN EoS is trained on density data generated with a volumetric model developed previously by the current authors [23–25]. The volumetric model enables the predictive generation of $P\rho T$ data, on which our ECS model was subsequently trained. Since the volumetric model needs no more than one experimental saturated liquid density

Table IV. Residual Functions' Prediction Accuracy (%) with Inversion for ECS–NN Trained on Data Generated from DEoS[a]

	Z			a^R			u^R			h^R			s^R			g^R			$\ln \varphi$		
Fluid	Vap.	Liq.	Sup.	Vap.	Liq.	Sup.	Vap.	Liq.	Sup.	Vap.	Liq.	Sup.	Vap.	Liq.	Sup.	Vap.	Liq.	Sup.	Vap.	Liq.	Sup.
R11	0.27	0.05	0.41	1.28	0.14	1.83	3.72	0.65	2.83	2.87	0.60	1.99	5.89	1.22	5.02	1.29	0.12	1.38	1.06	0.54	1.81
R22	0.11	0.03	0.20	0.55	0.05	0.56	2.32	0.25	0.65	1.83	0.23	0.47	3.57	0.46	1.19	0.59	0.04	0.43	0.48	0.26	0.52
R32	0.37	0.14	0.37	1.33	0.13	0.52	2.64	0.36	1.75	2.25	0.33	1.38	3.49	0.63	2.71	1.25	0.11	0.53	1.15	0.26	0.42
R123	0.18	0.03	0.38	0.69	0.24	0.43	1.90	0.49	0.83	1.57	0.45	0.72	2.69	0.82	1.12	0.71	0.16	0.38	0.58	0.73	0.25
R125	0.20	0.03	0.39	0.75	0.23	2.07	3.62	0.45	4.81	2.72	0.42	3.37	5.94	0.78	9.65	0.74	0.19	1.49	0.65	0.44	2.22
R152a	0.35	0.05	0.50	1.21	0.14	0.74	2.41	0.28	0.48	2.03	0.26	0.47	3.15	0.58	0.51	1.18	0.11	0.62	1.01	0.24	0.69
Avg.	0.24	0.06	0.36	0.97	0.15	1.13	2.78	0.41	2.19	2.21	0.38	1.59	4.15	0.75	3.98	0.96	0.12	0.88	0.82	0.41	1.11

[a] Vap., vapor; liq., liquid; sup., supercritical.

Table V. Prediction Accuracy (%) at Saturation for ECS–NN Trained on Data from DEoS

Fluid	Sat. vapor pressure	Sat. liquid density	Sat. vapor density
R11	0.650	0.189	1.162
R22	0.239	0.098	0.700
R32	0.432	1.155	1.392
R123	0.865	0.120	1.415
R125	0.993	0.147	1.155
R152a	0.651	0.536	1.203
Avg.	0.638	0.374	1.171

value, the great advantage of this approach is predictivity. For developing this new model a method quite similar to the one described in the former case for "exact" density data was assumed. For the predictive volumetric model [23–25] the fluids R12 and R134a were selected as references.

For sake of brevity it is preferable not to report here all the weighting factors sets of the ECS–NN EoSs developed for each of the fluids studied, but, aiming at giving a single example, the weighting factors for R152a are listed in Table VI. The final values of the objective functions $f_{ob,2}$, $f_{ob,3}$, and $f_{ob,overall}$, Eqs. (26), (27), and (29), of the ECS–NN EoS are also reported in Table VI with respect to the residual compressibility factor Z^R and the vapor pressure P^{sat} coming from the predictive density model [25] and an ancillary equation [21], respectively. The corresponding values of the AADs, all over the regular grids for training, are 1.26% for Z^R and 1.35%

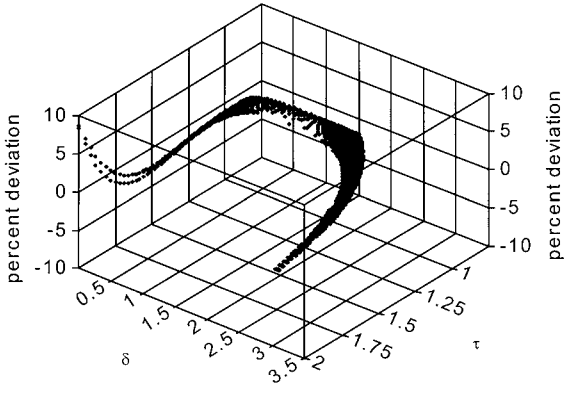

Fig. 2. Percentage error deviation on $a_j^R(\tau_j, \delta_j)$ for R152a. The ECS–NN model is trained on data generated from DEoS.

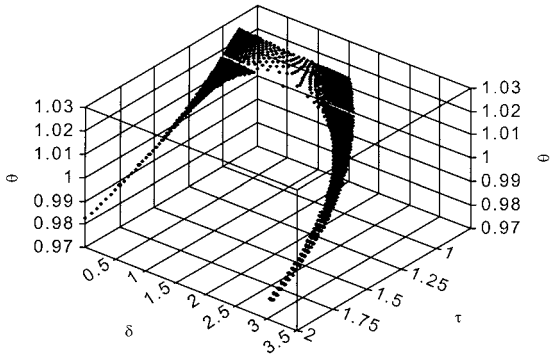

Fig. 3. Shape factor $\vartheta_j = \vartheta_j(\tau_j, \delta_j)$ for R152a. The ECS–NN model is trained on data generated from DEoS.

for P^{sat}, respectively. The resulting AAD values are considered to be quite satisfactory.

We compared the performance of our ECS–NN model, trained on data generated from the density model, with that of the Huber–Ely ECS model [3]. Both models aim for predictivity, though the latter also requires a saturated liquid volume correlation.

The validation results for our model are listed in Table VII. Because the density data used to train the model are less accurate than in the previous case, a certain drop in precision with respect to the former case is inevitable. This is evident for the supercritical region, in general, and particularly for R32, which is always the most difficult fluid to reproduce. The

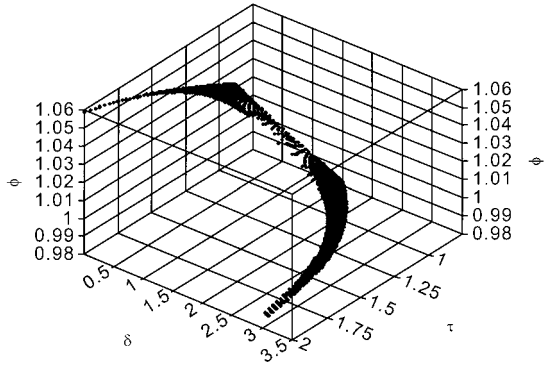

Fig. 4. Shape factor $\phi_j = \phi_j(\tau_j, \delta_j)$ for R152a. The ECS–NN model is trained on data generated from DEoS.

Table VI. Weighting Factors w_{ij} and w_{jk} and Parameters for the Shape Factors $\vartheta_j = \vartheta_j(T_{r,j}, \delta_j)$ and $\phi_j = \phi_j(T_{r,j}, \delta_j)$ of R152a

i	j	w_{ij}	j	k	w_{jk}
1	1	0.524453×10^{2}	1	1	-0.113905×10^{3}
2	1	0.190040×10^{3}	2	1	-0.427424×10^{2}
3	1	0.158936×10^{2}	3	1	0.158424×10^{2}
1	2	0.300692×10^{2}	4	1	-0.597281×10^{2}
2	2	0.121011×10^{3}	5	1	-0.174752×10^{3}
3	2	-0.383930×10^{2}	6	1	0.620108×10^{3}
1	3	0.753323×10^{2}	7	1	0.154052×10^{3}
2	3	0.248739×10^{3}	8	1	0.124274×10^{3}
3	3	-0.300739×10^{1}	1	2	-0.699742×10^{1}
1	4	-0.194355×10^{3}	2	2	0.379964×10^{2}
2	4	-0.232349×10^{3}	3	2	0.104075×10^{3}
3	4	-0.371052×10^{2}	4	2	-0.294540×10^{3}
1	5	-0.270544×10^{3}	5	2	0.680229×10^{2}
2	5	-0.120515×10^{3}	6	2	-0.297338×10^{3}
3	5	-0.565987×10^{2}	7	2	-0.211452×10^{3}
1	6	-0.161977×10^{3}	8	2	-0.116517×10^{3}
2	6	-0.947853×10^{3}			
3	6	-0.116044×10^{3}			
1	7	-0.186182×10^{2}			
2	7	-0.504267×10^{3}			
3	7	-0.106972×10^{3}			

Independent variables' extrema

$V_{\min,1}$	0.51
$V_{\max,1}$	1.13
$V_{\min,2}$	0.222280×10^{-3}
$V_{\max,2}$	0.309589×10^{1}

Dependent variables' extrema

$W_{\min,1}$	0.8
$W_{\max,1}$	1.2
$W_{\min,2}$	0.8
$W_{\max,2}$	1.2

Residual values of objective functions

$f_{\text{ob},2}$	0.153523×10^{-2}
$f_{\text{ob},3}$	0.861922×10^{-4}
$f_{\text{ob, overall}}$	0.139033×10^{-2}

Table VII. Residual Functions' Prediction Accuracy (%) with Inversion for ECS–NN Trained on Data Generated from the Density Model[a]

	Z			a^R			u^R			h^R			s^R			g^R			$\ln \varphi$		
Fluid	Vap.	Liq.	Sup.	Vap.	Liq.	Sup.	Vap.	Liq.	Sup.	Vap.	Liq.	Sup.	Vap.	Liq.	Sup.	Vap.	Liq.	Sup.	Vap.	Liq.	Sup.
R11	0.18	0.22	0.85	0.97	0.41	1.55	4.80	0.71	2.37	3.60	0.66	1.93	8.17	1.31	3.79	1.04	0.35	1.48	0.88	1.44	1.36
R22	0.15	0.18	0.78	0.49	0.08	1.08	1.69	0.27	0.55	1.25	0.25	0.41	2.96	0.46	1.33	0.49	0.09	1.18	0.43	0.48	0.44
R32	0.85	1.59	7.31	3.08	1.26	12.3	10.5	2.96	3.83	7.75	2.63	4.61	17.1	5.98	5.18	3.23	1.07	11.7	2.59	2.00	10.0
R123	0.12	0.30	0.80	0.80	0.27	0.85	3.08	0.42	0.64	2.45	0.39	0.62	4.60	0.83	0.73	0.81	0.25	0.82	0.74	0.95	0.51
R125	0.15	0.36	2.04	1.79	0.39	3.44	3.20	0.69	5.31	2.37	0.61	4.24	5.45	1.29	9.67	1.62	0.35	3.53	1.78	0.63	2.79
R152a	0.33	0.70	2.60	1.94	0.50	2.74	6.02	0.96	1.51	4.85	0.87	1.34	8.49	1.72	2.41	1.91	0.41	2.53	1.78	0.62	1.76
Avg.	0.27	0.56	2.55	1.50	0.49	4.10	4.87	1.00	2.67	3.70	0.90	2.47	7.77	1.93	4.38	1.50	0.42	3.98	1.36	1.02	3.21

[a] Vap., vapor; liq., liquid; sup., supercritical.

Table VIII. Prediction Accuracy (%) at Saturation for ECS–NN Trained on Data from the Density Model

Fluid	Sat. vapor pressure	Sat. liquid density	Sat. vapor density
R11	1.086	1.876	1.716
R22	0.341	0.212	0.674
R32	2.984	0.312	4.728
R123	0.869	0.128	1.381
R125	1.34	0.144	1.890
R152a	1.351	0.733	2.109
Avg.	1.325	0.567	2.083

volumetric precision is very good in the vapor and liquid phases, with an average AAD less than 0.3 and 0.6%, respectively, but in the supercritical region it rises to over 2.5%. Generally speaking, the results obtained for the various residual potential functions vary from fluid to fluid and also from one region to another. The functions' AADs in the liquid zone are around 1%, while the AAD for the supercritical and vapor regions falls between 1 and 4%, with only one case exceeding these values, i.e., s^R in the vapor phase, where an AAD of 7.8% is reached. The validation results of the ECS–NN model on the saturation line are listed in Table VIII; also, in this case the prediction accuracy is worse, with error deviations larger by a factor of about two. The validation of the Huber–Ely [3] ECS model is presented in Table IX. The AAD on $P\rho T$ data is about 0.5% for the liquid and less than 1.5% for the vapor and supercritical regions. The residual potential functions AADs in the liquid zone are usually less than 1.5%, while the AADs in the vapor phase are significantly higher, generally between 8 and 15%, with the highest value, for s^R, reaching nearly 20% as the mean value. In the supercritical region the AAD values are usually limited to 5% at the maximum. Results of the validation tests along the saturation line are listed in Table X; the results for density are, in particular, worse.

7. CONCLUSIONS

A new method for determining shape factors in the ECS modeling framework is proposed. The approach requires an a priori analytical form for the shape factor functions, and, for this, the ANN, as very versatile function approximators, have been applied. The shape factors are represented through ANN as functions of the two independent variables, temperature and density. The ECS–NN EoS parameters are determined trough

Table IX. Residual Functions' Prediction Accuracy (%) for the Conventional ECS Model [3][a]

	Z			a^R			u^R			h^R			s^R			g^R			$\ln \varphi$		
Fluid	Vap.	Liq.	Sup.	Vap.	Liq.	Sup.	Vap.	Liq.	Sup.	Vap.	Liq.	Sup.	Vap.	Liq.	Sup.	Vap.	Liq.	Sup.	Vap.	Liq.	Sup.
R11	1.67	0.65	1.13	12.5	0.96	2.95	23.3	1.40	3.46	19.5	1.32	3.07	32.6	2.75	4.41	11.9	0.87	2.64	11.6	2.92	2.99
R22	0.75	0.21	0.45	5.31	0.32	0.97	8.91	0.64	1.78	7.61	0.60	1.46	11.4	1.17	2.36	5.06	0.29	0.90	4.91	1.36	1.03
R32	2.57	0.96	2.40	14.7	1.02	6.19	20.3	1.02	7.07	18.6	0.89	6.49	23.8	2.67	8.62	14.1	0.92	5.57	13.6	1.56	5.81
R123	0.80	0.51	0.81	14.7	1.02	6.19	10.8	0.73	2.71	9.10	0.69	2.16	14.2	1.28	3.70	5.36	0.46	1.15	5.10	1.33	1.10
R125	0.91	0.50	1.19	5.30	0.46	2.50	15.8	0.90	7.99	12.6	0.84	5.82	23.5	1.60	14.9	5.28	0.45	2.23	4.72	0.72	1.67
R152a	1.14	0.45	0.92	7.03	0.70	1.69	10.5	1.35	1.85	9.47	1.25	1.76	12.7	1.97	2.18	6.72	0.59	1.49	6.51	1.45	1.90
Avg.	1.14	0.45	0.92	8.41	0.66	2.85	14.1	1.01	4.59	12.8	0.93	3.82	19.8	1.91	6.78	8.07	0.60	2.57	7.75	1.56	2.84

[a] Vap., vapor; liq., liquid; sup., supercritical.

Table X. Prediction Accuracy (%) at Saturation for the Conventional ECS Model [3]

Fluid	Sat. vapor pressure	Sat. liquid density	Sat. vapor density
R11	1.079	3.355	5.418
R22	0.647	2.384	4.064
R32	0.661	4.438	7.445
R123	0.701	2.835	4.739
R125	1.705	2.407	3.151
R152a	3.032	3.643	7.54
Avg.	1.304	3.177	5.392

a minimization procedure. A number of halogenated alkanes for which DEoS are presently available were considered in the study. The capability of the ECS–NN EoS to represent $P\rho T$ data in the vapor, liquid, and supercritical regions was verified, with an AAD between 0.026 and 0.5%, which is comparable to the analogous value of a multiparameter DEoS. The uncertainty of the model, trained on $P\rho T$ data, in representing residual potential functions was also tested, obtaining AAD values generally less than 0.8% for the liquid and less than 4% for the vapor and supercritical regions. The ECS–NN EoS was subsequently trained on $P\rho T$ data generated through an original predictive volumetric model requiring a single saturated liquid density value as input for each fluid. This makes the whole method predictive, although with an expected slight decrease in accuracy. The AAD values for $P\rho T$ data are much less than 1% in the liquid and vapor regions, while in the supercritical region they reach 2.5%. The AAD for residual potential functions are often less than 1% for the liquid and generally less than 4% for the vapor and supercritical regions. The comparison of the present predictive ECS–NN model with the Huber–Ely model [3] shows that in the liquid and supercritical regions the results are comparable, although not uniform for the second model, while the second model presents a marked deterioration in the representation of the vapor region residual potential functions.

The proposed model allows us to obtain an ECS model predictively, with locally defined individual shape factors, which shows good and consistent performance.

REFERENCES

1. T. M. Reed and K. E. Gubbins, *Applied Statistical Mechanics* (McGraw–Hill, New York, 1973).
2. J. S. Rowlinson and F. L. Swinton, *Liquids and Liquid Mixtures* (Butterworths, Oxford, 1982).

3. M. Huber and J. F. Ely, *Int. J. Refrig.* **17**:18 (1994).
4. J. S. Rowlinson and I. D. Watson, *Chem. Eng. Sci.* **24**:1565 (1969).
5. J. F. Ely, *Adv. Cryog. Eng.* **35**:1511 (1990).
6. R. Schmidt and W. Wagner, *Fluid Phase Equil.* **19**:175 (1985).
7. F. Rosenblatt, *Psychol. Rev.* **65**:386 (1958).
8. J. L. McClelland and D. Rumelhart, *Explorations in Parallel Distributed Processing*, 2 vols. (MIT Press, Cambridge, MA, 1988).
9. A. Normandin, B. Grandjean, and J. Thibault, *Ind. Eng. Chem. Res.* **32**:970 (1993).
10. C. Lombardi and A. Mazzola, *Ann. Nucl. Energy* **24**:1373 (1997).
11. R. Kühne, R. U. Ebert, and G. Schüürmann, *Chemosphere* **34**:671 (1997).
12. R. Sharma, D. Singhal, R. Ghosh and A. Dwivedi, *Comput. Chem. Eng.* **23**:385 (1999).
13. J. Homer, S. C. Generalis, and J. H. Robson, *Phys. Chem. Chem. Phys.* **1**:4075 (1999).
14. V. Kurkova, *Neural Networks* **5**:501 (1992).
15. R. T. Jacobsen, S. G. Penoncello, and E. W. Lemmon, *Fluid Phase Equil.* **80**:45 (1992).
16. S. G. Penoncello, R. T. Jacobsen, and E. W. Lemmon, *Fluid Phase Equil.* **80**:57 (1992).
17. A. Kamei, S. W. Beyerlein, and E. W. Lemmon, *Fluid Phase Equil.* **80**:71 (1992).
18. S. L. Outcalt and M. O. McLinden, *Int. J. Thermophys.* **16**:79 (1995).
19. S. G. Penoncello, R. T. Jacobsen, K. M. de Reuck, A. E. Elhassan, R. C. Williams, and E. W. Lemmon, *Int. J. Thermophys.* **16**:781 (1995).
20. R. Tillner-Roth and H. D. Baehr, *J. Phys. Chem. Ref. Data* **23**:657 (1994).
21. R. Tillner-Roth, *Int. J Thermophys.* **16**:91 (1995).
22. R. Fletcher, *Practical Methods of Optimization*, 2nd ed. (Wiley, Chichester, UK, 1987).
23. M. Grigiante, G. Scalabrin, and S. Bobbo, *Proc. 20th Int. Congr. Refrig.*, Sydney, Australia (1999).
24. G. Cristofoli, M. Grigiante, and G. Scalabrin, *Fluid Phase Equil.* **170**:23 (2000).
25. G. Scalabrin, M. Grigiante, G. Cristofoli, and L. Piazza, *Int. J. Refrig.*, submitted for publication.